A Time Resolved Study of Precoated AISI 441 for SOFC Interconnects using STEM-EELS – Part II

L. S. Karlsson[a], M. W. Lundberg[b], R. Berger[b], and J. Westlinder[b]

[a] Physical Metallurgy, AB Sandvik Materials Technology, 81181 Sandviken, Sweden
[b] Surface Technology, AB Sandvik Materials Technology, 81181 Sandviken, Sweden

Precoated AISI441 for SOFC interconnectors were investigated by STEM-EELS looking at the diffusion processes in the initial stage of the oxidation. The electron beam physical vapour deposition (EB-PVD) coating contained Ce and Co/Mn-alloy in two layers with at total thickness of 800 nm. The samples were exposed up to 1000 hours at 800°C, and then characterized by STEM-EELS. Multiple linear least squares (MLLS) fitting of reference spectra aids the interpretation of the elemental maps due to overlapping edges. Within 4 min heat treatment the oxidation front has reached the substrate steel and Cr_2O_3 is forming at the stainless steel interface. CeO_2 acts as the barrier line for Cr and is situated between the Cr-containing spinels and the (Co,Mn)-spinel after up to 168 h heat treatment.

Introduction

A solid oxide fuel cell (SOFC) is an electrochemical device which converts chemical energy in fuels into electrical energy. The fuel cell is containing an electrolyte sandwiched between a porous anode and a porous cathode. The fuel cell is then separated from the next by interconnects building up the SOFC stack. Today, most interconnects for SOFC are metallic and based on ferritic stainless steels. The properties that are the most important are high electronic conductivity, a thermal expansion coefficient similar to the surrounding adjacent ceramic components, and a thermal stability at service temperatures roughly spanning from 550°C to 1000°C. Water is a biproduct of the electrochemical conversion and thus an oxidation resistant material is required for the interconnector. Among the ferritic stainless steel candidates (alumina, chromia, or silica) only chromia formers are suitable as both alumina and silica form insulating protective scales (1,2). Steel producers and other developers have developed alloys with an expected lifetime of 40,000 hours, a coefficient of thermal expansion compatible with the ceramic components of SOFCs, good surface conductivity in the formed oxide scale etc. However, the specialized interconnector steel grades are still costly to manufacture due to the alloying elements and production routes and as a result, other ferritic stainless steel grades spanning from AISI430 to 446 have been considered.

Sandvik Materials Technology have been developing interconnector steels and surface coatings for interconnect steels for more than a decade. Co coatings, for instance, can be used to minimize detrimental chromium evaporation from ferritic stainless steel and to improve the electrical conductivity of the formed oxide scale (3). The idea is to deposit a metallic Co coating which will oxidize and react with Mn that diffuses from the substrate

to the Co coating, resulting in a CoMn-spinel at the surface on the interconnect. Except from substantially reducing the Cr evaporation (3) the formed CoMn-spinel will have a relatively good electrical conductivity (4). The thickness of the CoMn-spinel will be dependent of the initial thickness of the Co coating and it has been shown that up to a cobalt thickness around 600-800 nm the Cr evaporation is suppressed linearly with Co layer thickness. It has been shown that a small amount of Ce added to the spinel improves the ASR as well as reduces the mass gain due to less oxidation (4). Although the effect of the additional Ce layer is evident, the mechanism is not fully understood. Earlier studies (5,6) within the EU FP7 METSOFC project performed at Chalmers University of Technology have shown that nanocoatings of this type strongly decreases the oxidation rate and therefore improves the long term stability of the interconnect.

A time resolved study of Ce/Co-Mn coated AISI 441/0C365 strip steel intended for interconnects in solid oxide fuel-cells (SOFC) has been conducted within SMT R&D. In this study the combination of scanning transmission electron microscopy (STEM) and electron energy loss spectroscopy (EELS) is utilised for advanced materials characterisation in collaboration with the Kelvin Nanocharacterisation Centre, Glasgow University. As the amount of data collected is quite huge we have decided to divide the results into two papers for clarity and the readers benefit. However, we recommend reading the papers side by side.

Experimental

Cold rolled steel strip with a thickness 0.2 mm of a commercial ferritic stainless steel AISI441 were used in the present study. The nominal chemical composition is (in wt%): 17.8 Cr, 0.48 Nb, 0.26 Mn, 0.55 Si, 0.01, Ni 0.013, Ti 0.139. Closest to the stainless steel surface a 10 nm cerium layer was deposited by electron beam physical vapor deposition (EB-PVD) in a laboratory batch coater followed by a 600 nm thick co-evaporated manganese cobalt layer. The target value for the composition was 1:2 for the first 400 nm and then reversed, 2:1, for the remaining 200 nm, this to investigate the process control as well as to investigate how different areas diffuse after cyclic oxidation. Before coating deposition all substrates were cleaned in acetone and ethanol followed by alkaline cleaning at 60°C for 10 min. After alkaline cleaning the substrates were rinsed in hot tap water, deionized water and finally in ethanol. The uncoated substrates were cleaned in the same way before the oxidation experiments. The size of the double sided coated substrates was 15×30 cm. Sample coupons were cut with the dimensions 15 mm × 15 mm. A hole with 3 mm in diameter was punched into the sample for sample handling. Before exposure the samples were degreased and cleaned as previously described. The samples were mounted vertically on an alumina sample holder, and positioned parallel to the gas flow, in the center of a horizontal tube furnace. The furnace was operated at 800°C. The reaction gas consisted of 20% O_2, 77% N_2 and 3% H_2O. The volumetric flow rate was 1000 ml/minute, giving a linear flow rate of approximately 3.8 cm/s. Digital mass flow controllers were used for the dry carrier gases. For adding the water vapor, the dry gas flow was bubbled through a humidifier and cooled to the correct dew point (24.4°C for 3% water vapor) in a condenser, before being led into the furnace. All parts of the system downstream of the condenser were kept above the relevant dew point, in order to prevent condensation. One sample at 72 hours and 168 hours were prepared. The

sample exposed for 30 s was prepared by putting the sample in a muffle furnace in ambient air for 30 seconds for practical reasons.

The samples were subjected to heat treatment at 800˚C using certain time intervals with the moment the sample were put into the furnace as the starting point. After heat treatment the samples were prepared for TEM by FIB lift-out techniques using Pt as a protective surface layer subsequently mounted on Omniprobe grids. In this study the samples subjected to 30 s, 4 min, 72 h and 168 h heat treatment were characterised.

Data acquisition

STEM-EELS data cubes were acquired on the JEM-ARM200F at the Kelvin Nanocharacterisation Centre using a 200 kV beam with 0.1-1 nm probe size with simultaneous low-loss and core-loss acquisition a k a dual-EELS mode. Reference images were acquired using the high-angular annular dark-field (HAADF) detector to generate images with atomic number (Z) contrast. In these reference images the area for the 3D data cube and drift correction were assigned before acquisition.

Data processing – Part I

After acquisition the data-sets were corrected using a fresh dark reference to compensate for any change in background caused by the intensity of the acquired spectra on the CCD. Before further analysis energy drift was corrected for using the zero-loss peak (ZLP) in the low-loss spectrum image (SI) and the O-K edge in the core-loss SI. Any thickness related effects were removed by deconvolution using the ratio method in order to remove the plural scattering in the EELS data. After this, x-rays were removed from the volume of the deconvoluted SI. Elemental maps were extracted using the dynamic map option with carefully selected background and signal windows to match the conditions of the full region of interest as closely as possible. Due to overlapping of neighbouring peaks this was not always successful and multiple-linear least-squares (MLLS) fitting to reference spectra with known peaks were performed. In this case, an energy window (575 - 920 eV) including all the peaks of interest (Table I) was chosen using reference spectra from the EELS-atlas (Cr, MnO_2, CoO and CeO_2). Ideally, the reference spectra should be acquired using materials of known composition and thickness at similar acquisition conditions but at this point all of the materials were not available to us and reference spectra from the EELS-atlas was used.

TABLE I. EELS-edges of interest in the MLLS-fitting.

Element	**L_3-edge**	**L_2-edge**
Cr	575	584
Mn	640	651
Co	779	794

Data processing – Part II

Further data analysis was done by calculating multivariate histograms from MLLS fit coefficients to identify areas of specific phases. This technique can often identify regions

of compositional correlation not necessarily detectable by eye. Finally, the white-line ratio of the different phases was determined from the extracted EELS-spectrum of a given phase identified by the trivariate histogram. The white line ratio could be determined using the *Double Atan EELS Background* script (7) method or the second derivative method depending on the method used in the reference literature (8,9).

Results and discussion

30 s

The trivariate diagram of the Cr, MnO_2, and Co MLLS fit coefficients (Part I, Figure 1) identifies the Pt capping layer labelled region of interest 1(ROI 1), the upper oxide (ROI 2), the substrate steel and the C-rich interface (ROI 3), the Mn-rich (ROI4) and Co-rich (ROI5) metal layers (Figure 1). Note that the Cr content in the Pt capping layer and the upper oxide is an artefact of the MLLS fitting and will not be considered. However, the substrate steel (ROI 3) has a real Cr content of 17,8%. Interestingly, the Mn-rich metal layers (ROI 4) has a very distinct composition while the Co-rich metal layers show a variation in composition along the CoO-MnO_2 edge of the diagram. As the deposition of Mn is off-set compared to Co during coating the Co content is likely to gradually increase towards the top of the layered structure.

The O K-edge fine structure changes dramatically between the oxide above and below the C-rich contamination layer (Figure 2) where the first characteristic peak at 536 eV is completely missing under the C-rich contamination layer and instead an additional peak at 566 eV is present. Such a change in the O K-edge fine-structure has previously been observed when changing the B^{3+} cation in the normal spinel (10) e g Al^{3+} instead of Cr^{3+}. The white-line ratios of Mn L_3/L_2 and Co L_3/L_2 for the two oxides does indeed reflect a change in cation valency between the two regions where the protruding oxide contains Mn^{2+} and Co^{2+} and the upper oxide contains Mn^{3+} and 1/3 Co^{2+} + 2/3 Co^{3+}. This is probably an effect of the oxidation front progressing through the coating layers and would be interesting to correlate to crystal structure. This would clarify whether the spinel structure can form before the correct valence states are reached.

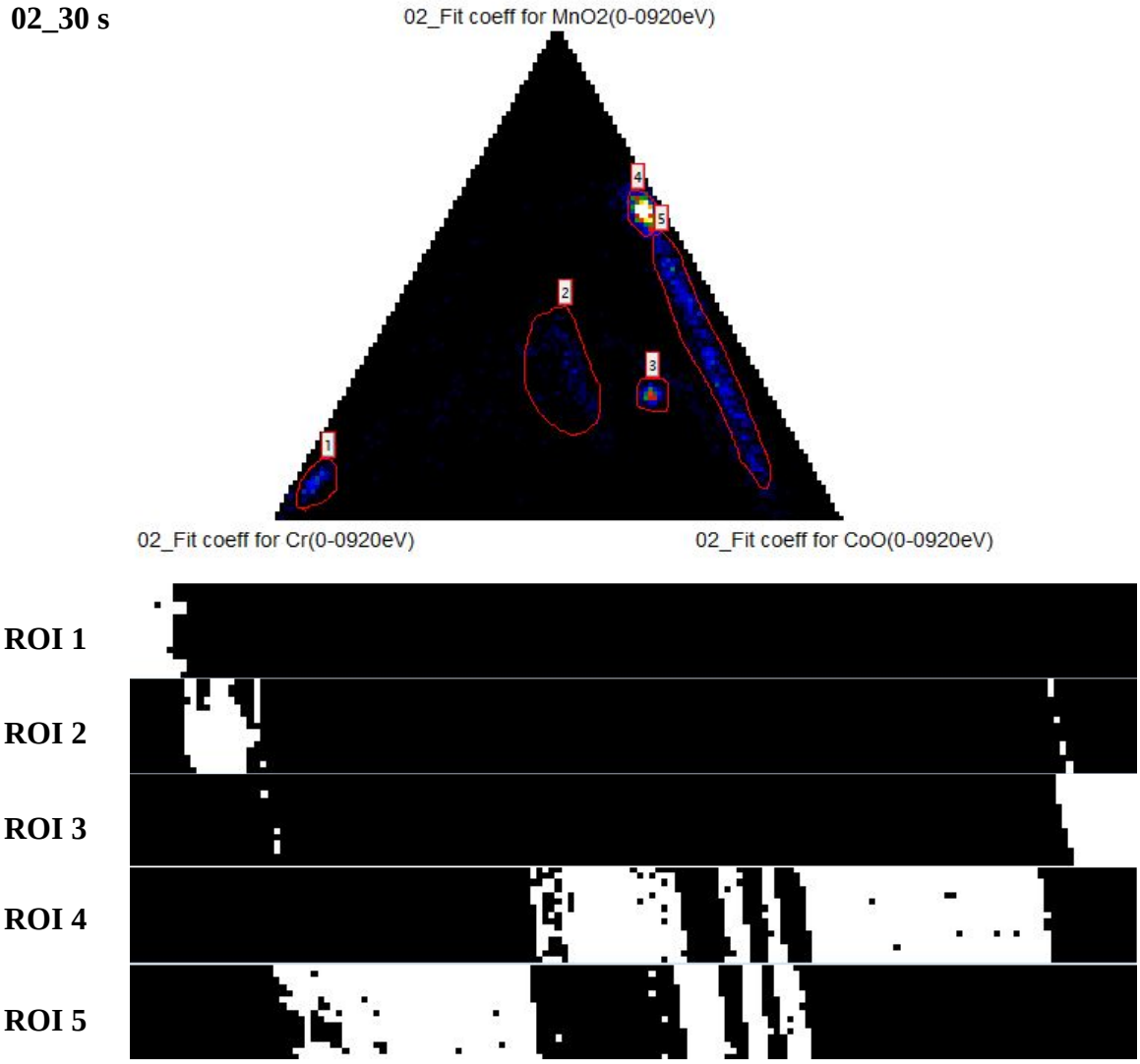

Figure 1. Trivariate diagram of Cr, MnO_2 and CoO fit coefficient maps of 02_30 s (Part I, Figure 1) showing five distinct regions: Pt capping layer (ROI 1), upper oxide (ROI 2), steel substrate (ROI 3), Mn-rich coating (ROI4) and Co-rich coating (ROI 5)

O K

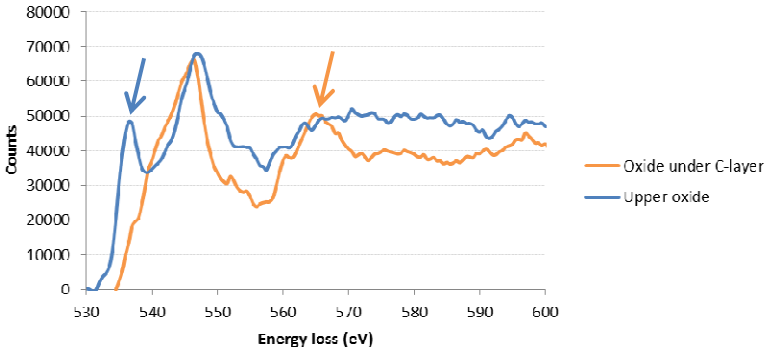

Mn L

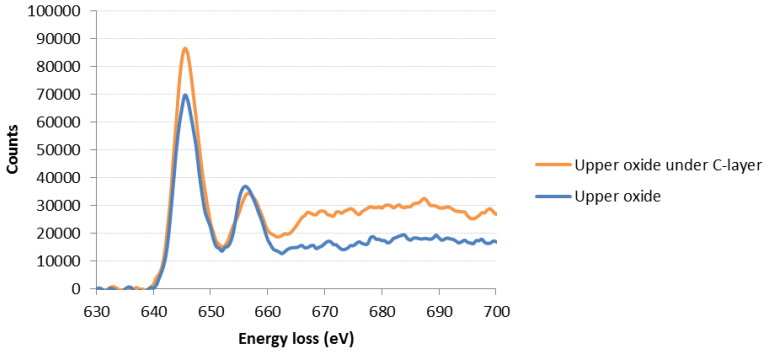

Co L

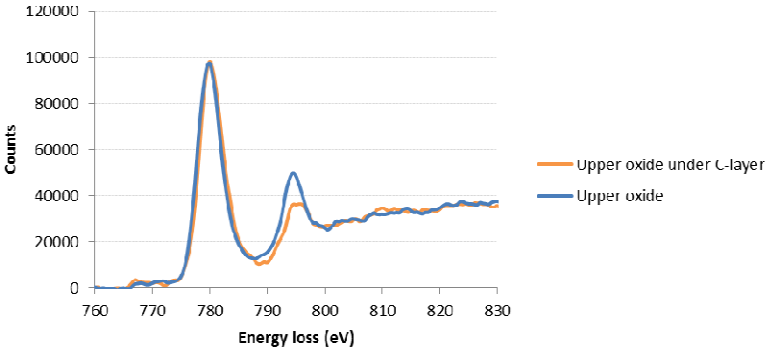

Figure 2. Changes in the O K-edge fine structure indicates that the upper oxide (blue) and the oxide under the C-layer have different cation species. White-line ratios of Mn L_3/L_2 and Co L_3/L_2 confirms that the upper oxide contains Mn^{3+} and 1/3 Co^{2+} + 2/3 Co^{3+} and the oxide under the C-layer consist of Mn^{2+} and Co^{2+}.

<u>4 min</u>

Using the trivariate histogram routine regions of correlated composition can be identified (Figure 3). When correlating the fit coefficient maps of Cr, MnO_2 and CoO one can easily distinguish the Co-Mn layer (ROI1), the steel substrate (ROI2), the CrO_X layer (ROI3), the Mn-rich interface layer (ROI4) and the Ce-rich layer (ROI5). Most of these ROIs have well-defined compositions but the CrO_X -layer (ROI3) stands out with its elongated shape possibly most likely caused by the mobility of Cr in this region. As was noted in Part I the Mn-rich interface layer (ROI4) can be a result of an inclined interface

in the sample where an overlap between the steel substrate and the added coating gives this effect.

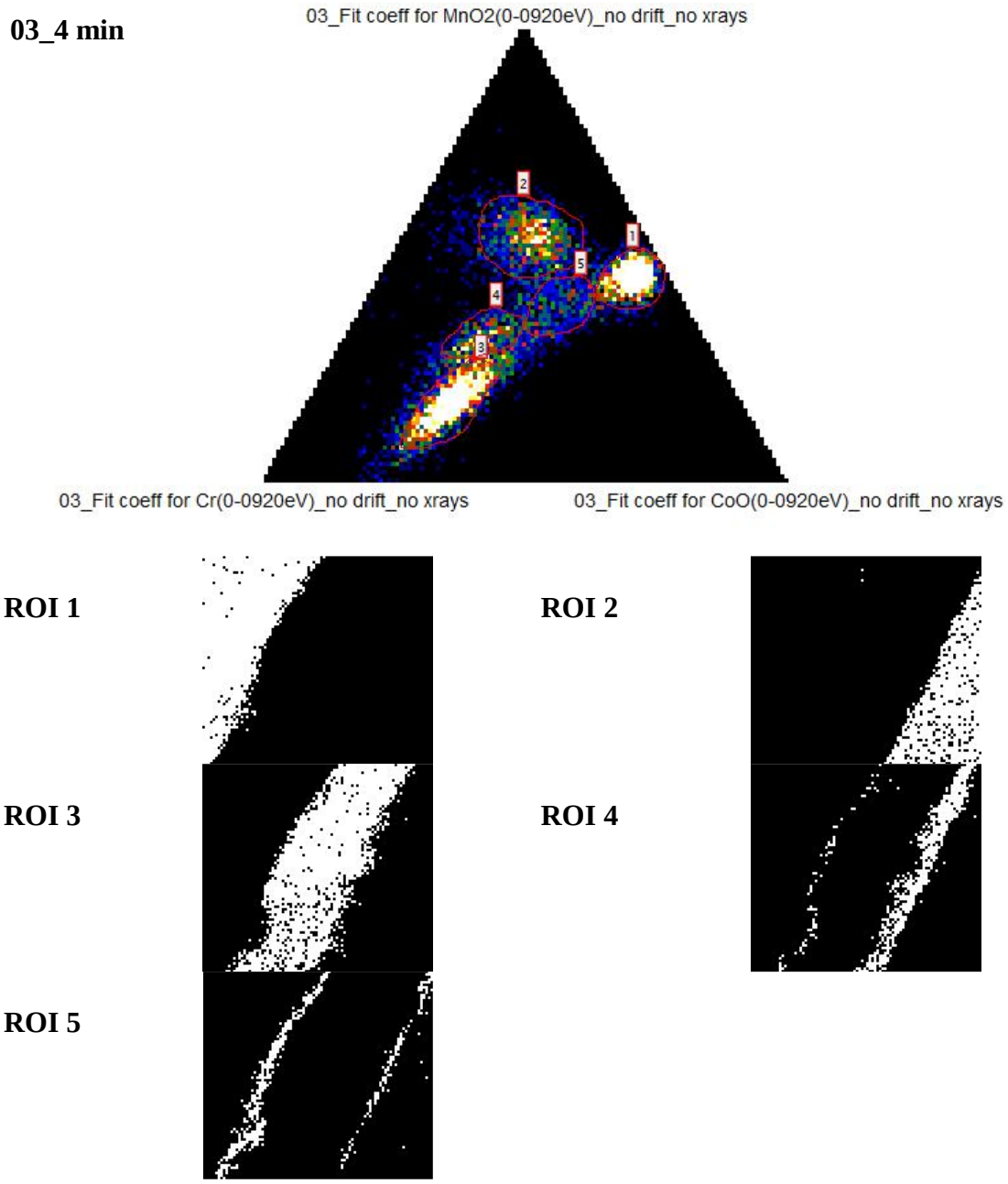

Figure 3. Trivariate diagram of Cr, MnO_2 and CoO fit coefficient maps of 03_4 min (Part I, Figure 2) showing five distinct regions: Co and Mn-rich metal (ROI 1), steel substrate (ROI 2), CrO_x (ROI 3), Cr-deficient and Mn-rich interface layer (ROI4) and trace values in the Ce-layer and steel interface layer (ROI 5)

As for the 30 s sample the differences in cation species is reflected in the O K edge fine structure (Figure 4). Where Cr_2O_3 shows the two characteristic peaks at 537 and 547 eV, and the Co-Mn layer a reduction in height of the first peak and an additional peak at

553 eV often found in spinels (10). The reduction in size of the first peak is commonly a result of changes in the trivalent cation species, B^{3+} as was seen at the oxide under the C-layer at the oxidation front after 30 s heat treatment (Figure 2) where only M^{2+}-ions are present.

ROI 3

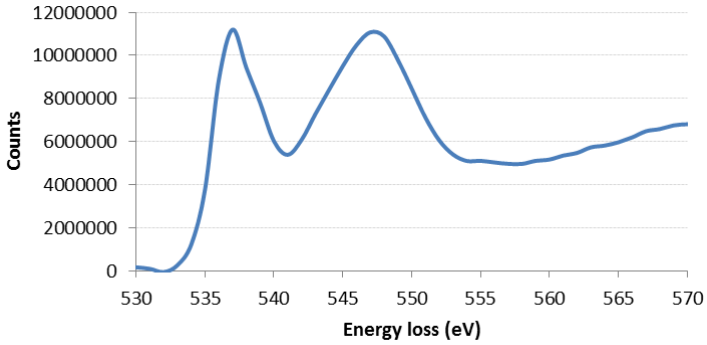

ROI 1

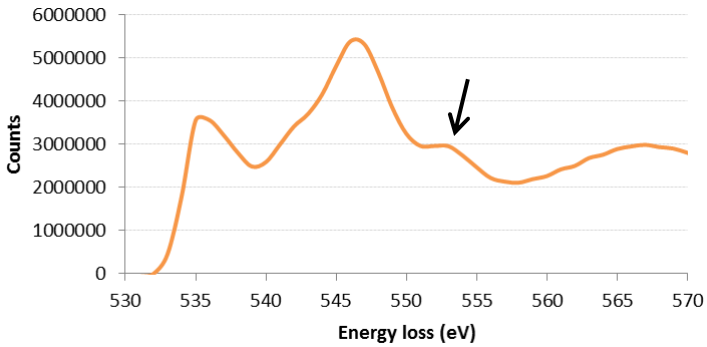

Figure 4. The O K-edge fine-structure of ROI 3 (Cr_2O_3) and ROI 1 (Co-Mn metal) reflects the changes in cation species in the different layers.

72 h

The trivariate histogram analysis (Figure 5) reveals not only that the Cr_2O_3 (ROI 1) and (Co, Cr)-spinel (ROI 2) can easily be distinguished but also that the region of (Co, Cr, Mn)-spinel grains (ROI3-5) can be split into three different grains based on composition with decreasing Cr content away from the stainless steel interface. Moreover, the CeO_2-particle is found situated at the grain boundary of these three grains. It should also be noted that the Cr content of the phases becomes more and more defined the further away from the steel substrate they are based. As was noted for the 30 s sample this is most likely an effect of the Cr evaporation from the steel.

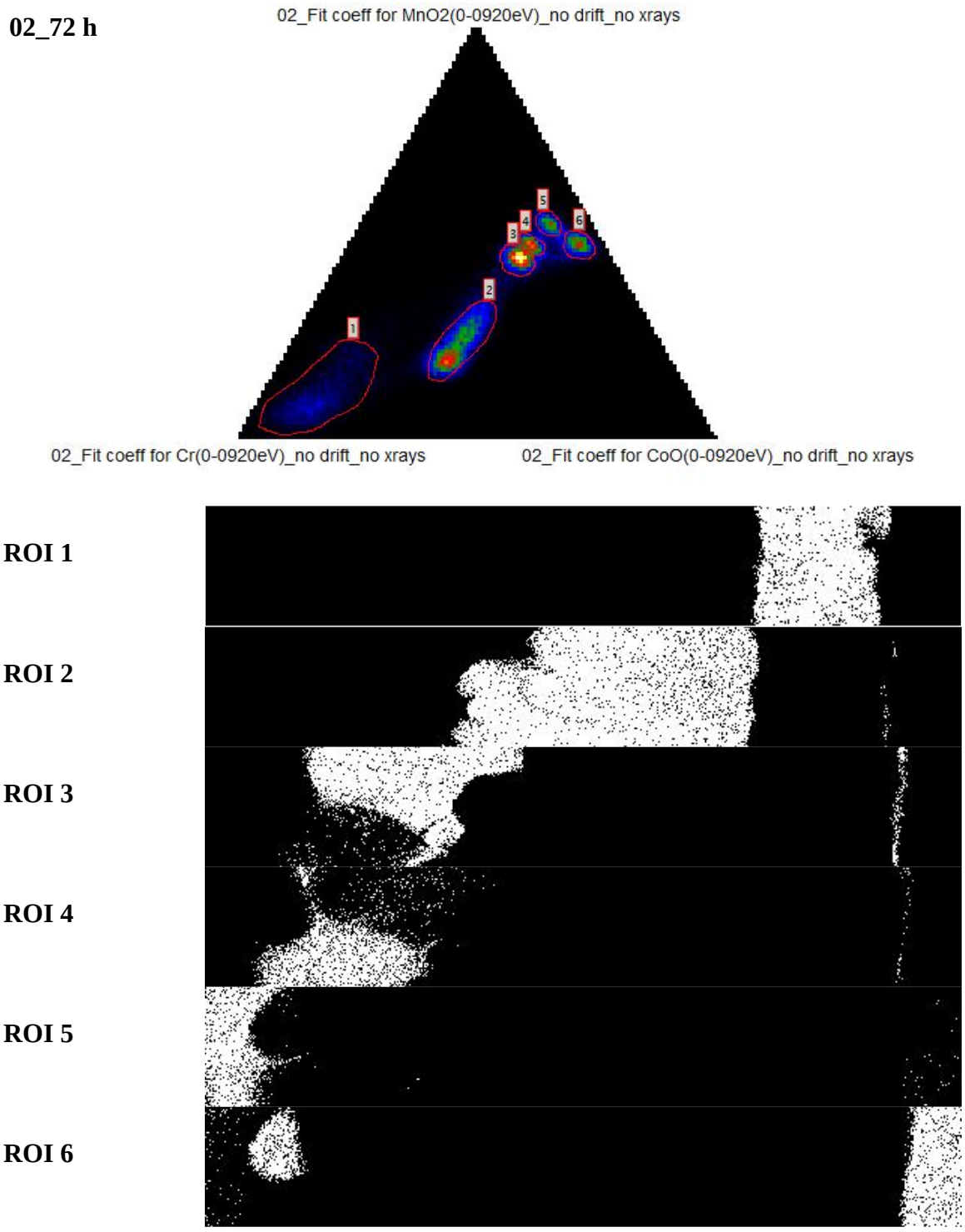

Figure 5. Trivariate diagram of Cr, MnO_2 and CoO fit coefficient maps of 02_72 h (Part I, Figure 3) showing six distinct regions: CrO_x (ROI1), (Co,Cr)-spinel (ROI2), (Co,Mn,Cr)-spinel (ROI3-4), (Co,Mn)-spinel (ROI5) and steel substrate (ROI6).

The fine-structure of the O K-edge (Figure 6) reflects the change in cation species with a gradual decrease in the first peak as the Cr^{3+} content decreases. Moreover, the characteristic peak at 552 eV is found for all the spinel grains (ROI2-5) and the relative

peak height distinguishes (Co,Cr)- from the (Co,Cr,Mn)- and (Co,Mn)-spinels. It should be noted that the relative peak height is the same for Cr_2O_3 (ROI 1) and the (Co,Cr)-spinel (ROI 2) but shows a shift in position of the second peak (A) from 547 to 546 eV. This probably reflects the small change in trivalent cation species, B^{3+} and presence of Co^{2+} in this structure.

ROI 1

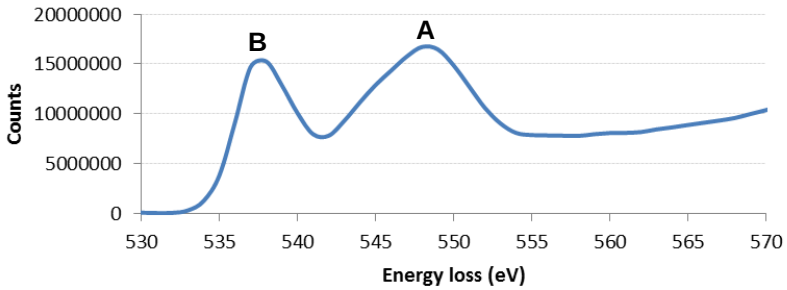

ROI 2

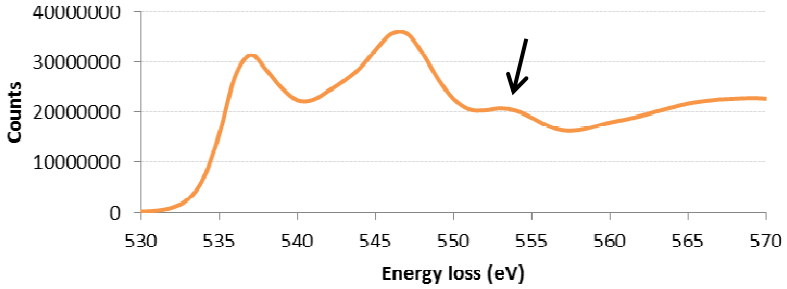

ROI3-4

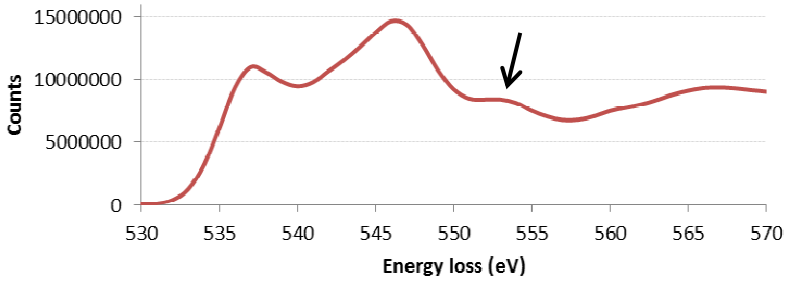

ROI5

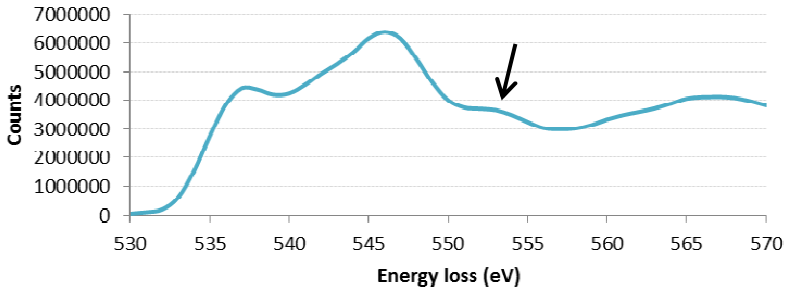

Figure 6. The O K-edge fine-structure of ROI 1-6 (Figure 5) reflects the changes in cation species in the different layers: CrO_x (ROI1), (Co,Cr)-spinel (ROI2), (Co,Mn,Cr)-spinel (ROI3-4), and (Co,Mn)-spinel (ROI5).

168 h

The trivariate histogram (Figure 7) cannot fully distinguish between the Cr_2O_3 (ROI 1) and the (Co,Cr)-spinel (ROI 3) and defines an intermediate phase at the interface (ROI2). This is most likely an effect of an inclined interface with overlapping phases as was observed for the steel substrate after 4 min heat treatment (Figure 3). The (Co, Cr, Mn)-spinel is defined as one single phase (ROI 4) and no longer distinguishes individual grains as was found after 72 h heat treatment (Figure 5). In this particular region of interest only one single grain of (Co,Cr,Mn)-spinel is included, so this observation is not such a surprise after all. However, the transition to the (Co, Mn)-spinel above the CeO_2-particle, as was observed at 72 h, is not at all clear. Either the (Co,Mn)-spinel front no longer coincides with the band of CeO_2 particles or the sample preparation has removed a neighbouring (Co,Mn)-spinel grain.

The O K-edge fine structure (Figure 8) is more or less identical for ROI1-2 and confirms the suspicion of an overlap region where Cr_2O_3 dominates. For the (Co,Cr)-spinel (ROI 3) the characteristic spinel peak at 552 eV appears and is even more pronounced in the (Co,Cr,Mn)-spinel (ROI 4). Moreover, the first peak in the (Co,Cr,Mn)-spinel has a reduced height as was observed for the (Co,Mn)-spinel after 72 h heat treatment (Figure 6). This suggests that ROI 4 has a lower Cr-content than at 72 h and is becoming virtually indistinguishable to the (Co,Mn)-spinel. This would explain why the trivariate histogram method could not pin point the transition to the (Co,Mn)-spinel at the CeO_2-front but also shows that the Cr evaporation is effectively reduced. Also, the (Co,Cr)- and (Co,Cr,Mn)-spinels (ROI3-4) are equally confined in composition (Figure 7) while the Cr_2O_3 (ROI 1) still shows the most elongated trace in the histogram.

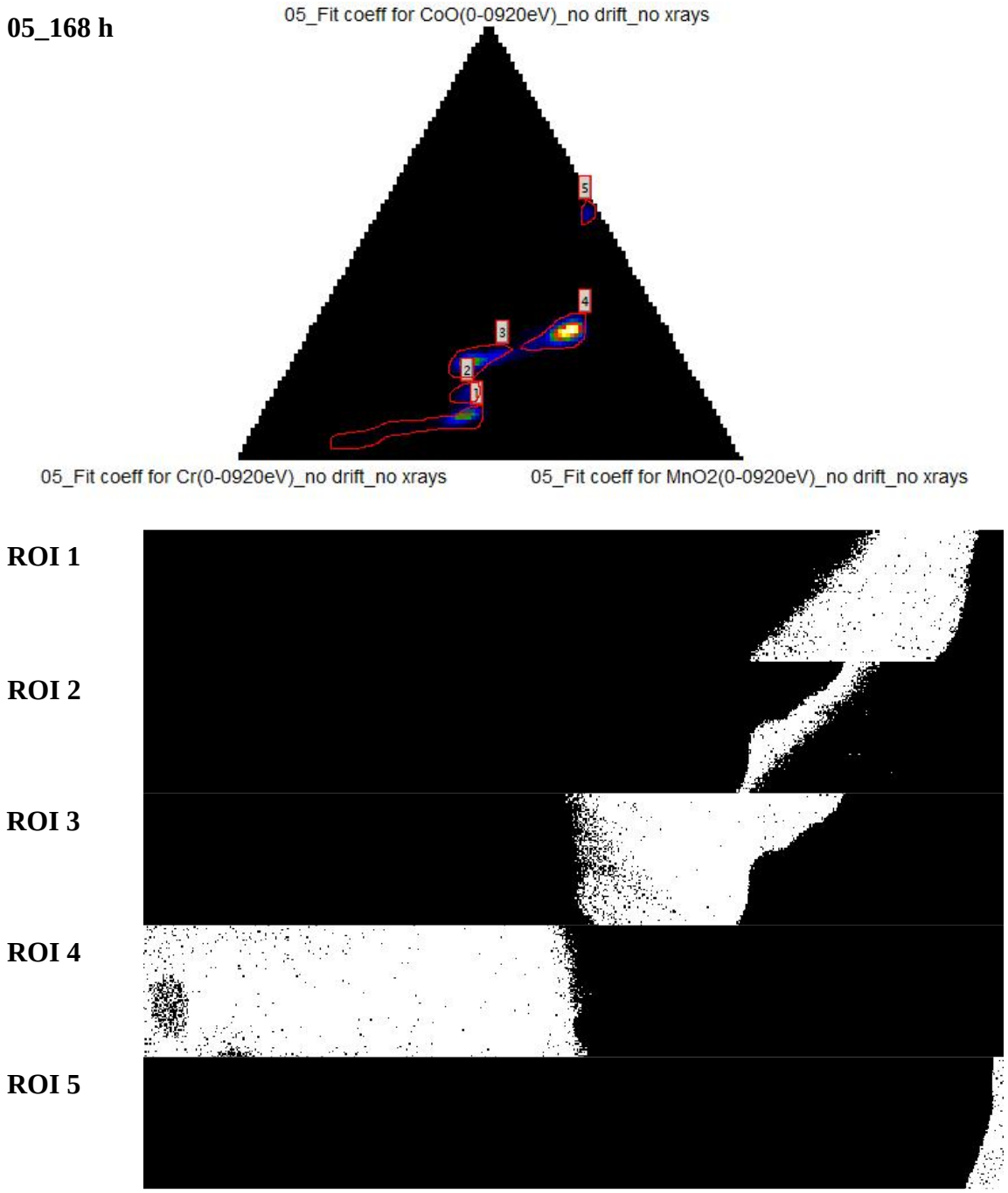

Figure 7. Trivariate diagram of Cr, MnO_2 and CoO fit coefficient maps of 05_168 h (Part I, Figure 4) showing five distinct regions: the Cr_2O_3 (ROI1), overlap region between Cr_2O_3 and (Co,Cr)-spinel (ROI2), (Co,Cr)-spinel (ROI3), (Co,Cr,Mn)-spinel (ROI4) and steel substrate (ROI 5)

ROI1

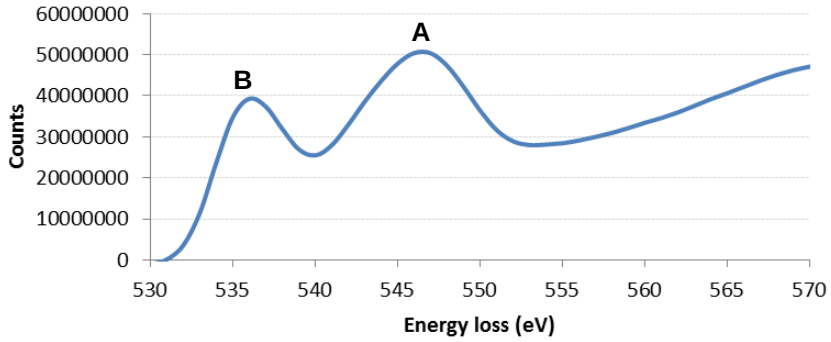

ROI2

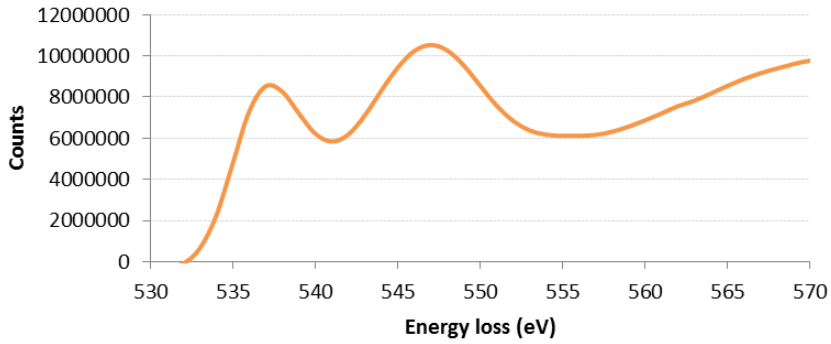

ROI3

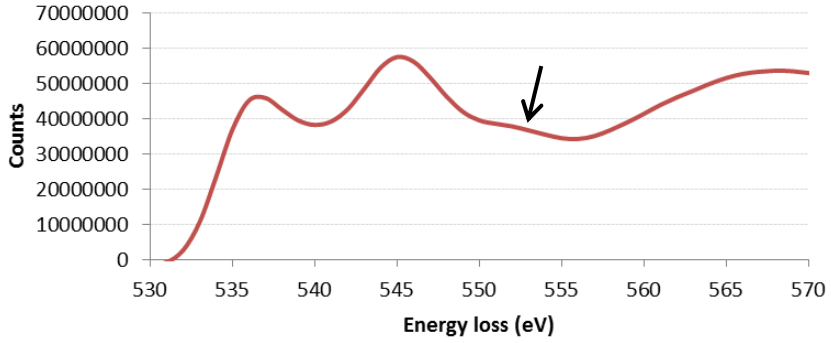

ROI4

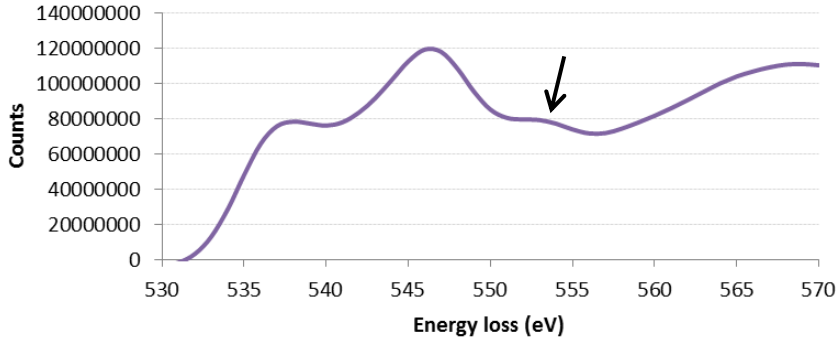

Figure 8. The O K-edge fine-structure of ROI 1-4 (Figure 7) reflects the changes in cation species in the different layers: ROI 1 (Cr_2O_3), ROI2 overlap region between Cr_2O_3 and (Co,Cr)-spinel, ROI3 ((Co,Cr)-spinel) and ROI4 ((Co,Mn, Cr)-spinel.

Conclusions

The use of STEM-EELS, MLLS-fitting and trivariate histograms gives truly added value to the acquired data. Not only can one distinguish phases not evident to the naked eye but the fine structure of relevant edges can be studied for each phase. However, care must be taken when the method defines unique phases as a result of overlapping regions, as was observed in several cases. Also, the mobility of the Cr is clearly seen on the shape of phase in the histogram and tends to decrease with distance from the steel substrate. Moreover, the fine structure of the O K-edge shows the development of the fully oxidised phases but can also distinguish between individual spinels based on differences in bonding alone. In combination with the white line ratios of the Cr, Co and Mn $L_{2,3}$ peaks the valence state of these elements can be determined for each phase and gives an even more complete picture of what is happening in this time resolved study. The ultimate experiment would be to perform this process in situ inside the TEM with relevant atmosphere to study the effects in real time. To summarize, we can conclude that by coating the steel with a (Co,Mn)-coating we are able to reduce the evaporation of Cr and Mn from the steel itself and therefore reduce the risk of embrittlement of the interconnect and in the long run increase the life time of the fuel cell stack.

Finally, we have showed it is possible to create and vary the composition of co-evaporated (Co,Mn)-alloy layer using EB-PVD in a laboratory scale setup. This could be used for more complex precoated layer structures for SOFC interconnects, which could be used to tailor-make the coating based on e.g. operating temperature requirements.

Acknowledgments

The research leading to these results has received funding from the Europeans Union's Seventh Framework Programme (FP7/2007-1013) for Fuel Cells and Hydrogen Joint Technology initiative within the project METSAPP, grant agreement n° [278257] 10, and within the project NELLHI, Grant Agreement n° [621227]. The authors would also like to acknowledge the Kelvin Nanocharacterisation Centre, Glasgow University.

References

1. N. Shaigan, W. Qu, D. G. Ivey and W. Chen, *J. Power Sources*, **195**, 1529 (2010)
2. J. W. Fergus, *Mater. Sci. Eng. A*, **A397** , 271 (2005).
3. N. Shaigan, PhD Thesis, University of Alberta 2009, http://hdl.handle.net/10048/402.
4. U. Bexell, M. Schuisky, H. Ravash, J. Froitzheim, J.-E. Svensson, Proc. of the 9th European SOFC Forum, Lucerne, Switzerland, 29 June-2 July 2008.
5. S. Canovic, J. Froitzheim, R. Sachitanand, M. Nikumaa, M. Halvarsson, L.-G. Johansson and J.-E. Svensson, *Surface and Coatings Technology*, **215**, 62 (2013).
6. J. Froitzheim, S. Canovic, M. Nikumaa, R. Sachitanand, L.G. Johansson and J. E. Svensson *J. of Power Sources*, **220**, 217 (2012).
7. D.R.G. Mitchell. *Double Atan EELS Background*. 20121124 v1.0 Available from: http://www.dmscripting.com/double_atan_eels_background.html.
8. T. L. Daulton and B. J. Little, *Ultramicroscopy*, **106**, 561 (2006).
9. Z. L. Wang, J. S. Yin, and Y. D. Jiang, *Micron*, **31**, 571 (2000).
10. D. A. Eustace, D. W. McComb, and A. J. Craven *Micron*, **41**(6), 547 (2010).